

Laura's Thesis oh yah

A Dissertation

Presented to

The Faculty of the Graduate School of Arts and Sciences

Brandeis University

Department of Physics

Professor Gabriella Sciolla, Advisor

In Partial Fulfillment

of the Requirements for the Degree

Doctor of Philosophy

by

Laura Bergsten

July, 2020

This dissertation, directed and approved by Laura Bergsten's committee, has been accepted and approved by the Graduate Faculty of Brandeis University in partial fulfillment of the requirements for the degree of:

DOCTOR OF PHILOSOPHY

Eric Chasalow, Dean of Arts and Sciences

Dissertation Committee:

Professor Gabriella Sciolla, Chair

Craig Blocker

Alessandro Tricoli

©Copyright by

Laura Bergsten

2020

For my family

Acknowledgments

This is to thank all the people. Gabriella and committee. Gaetano and Alessandro. All group members. Friends and family for sanity.

Abstract

Laura's Thesis oh yah

A dissertation presented to the Faculty of
the Graduate School of Arts and Sciences of
Brandeis University, Waltham, Massachusetts

by Laura Bergsten

The Higgs boson is measured by me in a channel it is nice and I graduate call me doctor

Contents

Abstract	vi
1 Introduction	1
2 Theory	2
2.1 Standard Model	2
2.2 History of SM tests	6
2.3 LHC Physics/Phenomenology	6
2.4 Measurement motivation	6
3 The LHC and the ATLAS detector	7
3.1 The Large Hadron Collider	7
3.2 A Toroidal LHC ApparatuS	9
3.3 The High-Luminosity LHC and Inner Tracker (ITk)	11
4 Tracking and Isolation in ATLAS	14
4.1 Tracking and isolation in ATLAS	14
5 Event Selection	26
5.1 Data and Monte Carlo samples	26
5.2 Object definitions	26
5.3 Event selection	26
6 Backgrounds and Systematics	27
6.1 Backgrounds	27
6.2 Systematic uncertainties	27
7 Results	28
7.1 Statistical analysis	28
7.2 Unfolding	28
7.3 Results and ratio measurements	28

CONTENTS

8 Conclusions

29

Chapter 1

Introduction

Introduction to the thesis. Explain what u'll see.

Chapter 2

Theory

2.1 Standard Model

The Standard Model (SM) is the leading theory that describes interactions between particles at a subatomic scale. I begin with a brief summary of the SM itself beginning with brief descriptions of the fundamental particles and their forces before delving into a summarized mathematical formulation. Next, I discuss the history of the SM and crucial tests of the theory up until current work at the LHC. I will then outline some of the recent and current physics at the Large Hadron Collider (LHC) with a focus on Higgs boson measurements. Finally, I'll introduce my thesis' main focus, differential cross-section measurements of Vector-Boson-Fusion Higgs decaying into two W-bosons.

The Standard Model is one of the most successful scientific theories to date. Its predictions encompass all of the visible universe and continue to undergo careful testing. The SM combines three forces- electromagnetic, weak, and strong - into one elegant description. I'll follow in the steps of many before me and detail the theory through first introducing particles and forces. Next I will introduce the mathematical formalisms describing particle interac-

CHAPTER 2. THEORY

tions. This section uses mainly the following citationsMartin + Shaw and something else? and phenomenology book.

2.1.1 Particles and forces

The particles we define in high energy physics are the most minute portions of matter we're able to observe. They are generally considered point-like, have no internal structure, and cannot be further split. Each particle we can define has a unique set of quantum numbers and its own anti-particle (with the same mass and spin, but opposite electrical charge and quantum numbers).

Particles can split up into distinct groups- first bosons, with integer spin, and fermions, with half-integer spin. Bosons are 'force carriers' meaning when particles interact they exchange bosons. Fermions are at the heart of all conventional matter. Fermions can be split further into two categories- leptons and quarks. Quarks have fractional integer charge and interact strongly while leptons have integer charge and interact solely through the weak or electromagnetic forces. Both quarks and leptons are made of three generations of particles, each heavier and more unstable than the next. Charts showing quark/lepton families and their key quantum numbers are shown below. Each generation of quarks and leptons contains a particle doublet. Each lepton doublet contains a charged lepton and a neutrino while each quark doublet contains one $+2/3$ charged particle and one with a $-1/3$ charge. Each lepton and quark also has an anti-particle. All conventional, stable matter is made from the first generation of quarks and leptons.

There are four gauge bosons and one scalar boson predicted through the SM. These correspond to three fundamental forces in nature (the fourth, gravity, is so small on the scale of particle interactions as to not be considered). The strongest force on the subatomic

CHAPTER 2. THEORY

scale is the strong force- this is mediated by the gluon- and works primarily to bind quarks together to form composite particles like protons or neutrons. The electromagnetic force is about 60x weaker than the strong force and is mediated by the photon. This force accounts for all electric interactions like that between an electron and an atomic nucleus. Finally, the weak force (10^4 weaker than the EM) facilitates β -decay and is mediated by massive Z and W bosons. Before going into more detail on the gauge bosons and the forces they mediate, I'd be remiss not to mention the Higgs boson. The only scalar boson predicted by the SM, it has no charge or intrinsic spin. The Higgs gives mass to all other particles through Spontaneous Symmetry Breaking, which I'll expand on in later sections.

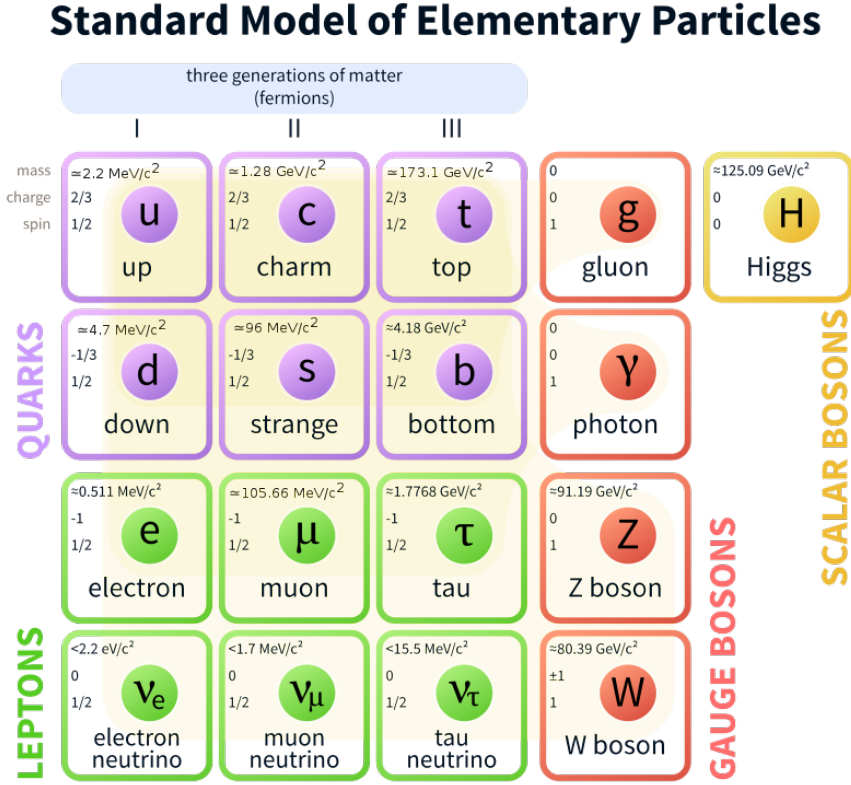


Figure 2.1: Three generations of quarks and leptons are shown along with all SM bosons (13)

Photons are massless, spin-1 particles and mediate all electromagnetic interactions. They couple directly to any particle with electric charge- so quarks, leptons, and W/Z bosons but not neutrinos. Since the photon is massless, the electromagnetic force can operate on infinitely long scales but its force decreases with $1/r^2$.

Gluons are massless particles with no charge and a spin-1. They couple to color charges, which are a property of quarks. Each quark has one of three colors (RGB) while anti-quarks have "anti" versions of these. Colors are conserved 'charges' just like electric charge. Quarks are never found alone as they couple so strongly to one another as to be confined in groups

CHAPTER 2. THEORY

of two or three. These groups are "color-confined" meaning the quarks contain colors which add up to a color neutral sum. For instance, a two quark meson $u\bar{u}$ may have colors R and anti-R while a three quark hadron uud (proton) may have colors R, G, and B. Gluons are different from photons in that they are not neutral to the charge they couple to. Gluons have two colors (8 total combinations) and can thus couple to each other. This makes the strong force distinct from the electromagnetic and has implications for long-distance interactions.

W and Z bosons, unlike gluons and photons, are massive. However, like their other gauge boson counterparts, they have spin-1 and mediate a charge (weak). W^\pm mediates charged-current interactions which can violate flavor conservation between quarks and/or leptons and their neutrinos. Z^0 mediates neutral-current interactions which conserve flavor. W^\pm bosons contain electric charge so can interact through EM as well. In addition, W and Z bosons contain weak charge (as do all fermions) so can self-couple as well as couple with all fermions.

The Higgs boson will be further motivated and described in later sections but suffice to say it's a massive spin-0 particle which couples to all particles with mass (including itself). It doesn't mediate any force but is still an integral part of the SM.

2.1.2 Gauge Invariance

Quantum electrodynamics, quantum chromodynamics and the unified electro-weak theory are all examples of gauge theories, which simply means they have gauge invariance symmetries.

CHAPTER 2. THEORY

2.1.3 Electroweak Unification

2.1.4 Spontaneous symmetry breaking

2.2 History of SM tests

2.3 LHC Physics/Phenomenology

2.4 Measurement motivation

Chapter 3

The LHC and the ATLAS detector

3.1 The Large Hadron Collider

The Large Hadron Collider (LHC) is the proton-proton storage ring operating at CERN and for last 13 years has been the world's highest energy particle collider. The LHC first began operation particles in 2008, but following a magnetic quench incident, it had to be repaired and adjusted, so the first data-taking didn't occur until 2009 (12). During the 9 years of LHC operation, protons colliding within each of the experiments were increased to larger center-of-mass energies, approaching the design energy of 14TeV. In addition, luminosity has successively been increased, surpassing design luminosity of $1 \times 10^{34} \text{cm}^{-2} \text{s}^{-1}$ in 2018 to reach $2 \times 10^{34} \text{cm}^{-2} \text{s}^{-1}$ (?). The overall data recorded in the ATLAS detector totals more than 10^{16} collisions. The consistent day-to-day operation of the LHC as well as its strides in increasing the energy and number of collisions produced has led to the most precise measurements of Standard Model constants including the coupling of the Higgs boson to bottom quarks (?), W and Z bosons (5), (7) as well as photons(6) and tau leptons (4). The LHC has also facilitated searches searches over a wide parameters space, setting confidence level exclusion

CHAPTER 3. THE LHC AND THE ATLAS DETECTOR

limits on masses of supersymmetric particles like squarks, gluinos and neutralinos (3).

The LHC is set to begin Run 3, in which design center-of-mass energy should be reached, in 2021. Following Run 3, detector upgrades will be made during a long shutdown and then the High-Luminosity LHC (HL-LHC), with unprecedented $10\times$ the luminosity of the LHC, will begin colliding protons in 2027(?). The HL-LHC and its goals will be explained further in ??, suffice to say that LHC-physics is progressing quickly and promises exciting developments in the near future.

In a brief explanation of the LHC operation, one could begin with the small volume of protons- numbering $\approx 10^{11}$ - that is accelerated. Next describe injection, acceleration in PS, SPS, then injection to LHC.

The LHC basic layout mimics that of the Large Electron Positron collider (LEP) that was housed in the same tunnels prior. Figure 3.1 shows the positioning of each experiment on the LHC as well as injection systems and other features. Once proton bunches enter the LHC in two opposing beams they are further accelerated with radio frequency systems. Located at Point 4 in the LHC schematic, the system consists of two cavities operating at twice the frequency of the SPS injector. **Brief explanation of RF cavity and how work**

Superconducting magnets in the LHC in the main dipoles of the create a magnetic field of $\approx 8\text{T}$ to bend the proton beams into the circular path of the collider. Figure 3.2 shows the flux in a dipole cross-section. The opposing direction beamlines are shown centered and the flux is shown to be high (and directionally opposed) in center of each beam. To maintain these fields, the magnets operate at below 1.9K. Pressurized superfluid helium, chosen for its low viscosity and high specific heat, cools the dipole magnets. Once the two LHC rings are filled from the SPS, center-of-mass energy of the beams increase until they reach peak energy after about 28 minutes. Finally, proton bunches separated by 25ns collide simultaneously in each detector.

CHAPTER 3. THE LHC AND THE ATLAS DETECTOR

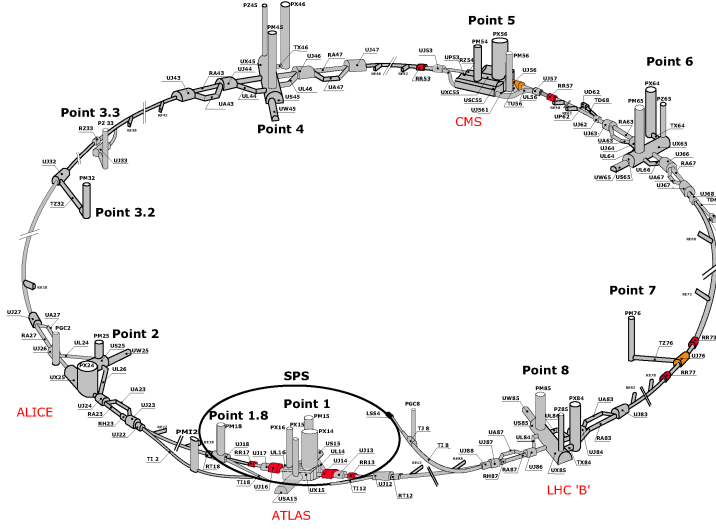


Figure 3.1: LHC layout [??]

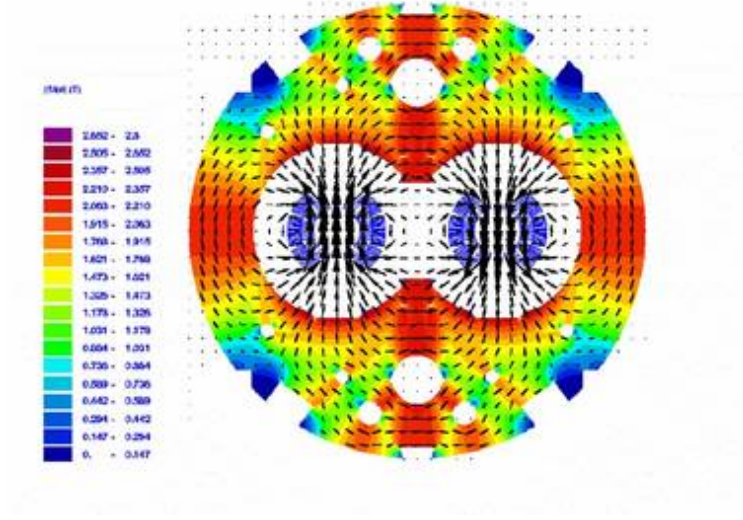


Figure 3.2: Flux within an LHC dipole cross-section [??]

3.2 A Toroidal LHC ApparatuS

The LHC creates proton-proton collisions at a rate and energy level key for pushing the boundaries of particle physics, but identifying and reconstructing the tracks of such energetic particles decay products is no mean feat. A Toroidal LHC ApparatuS (ATLAS)

CHAPTER 3. THE LHC AND THE ATLAS DETECTOR

and the Compact Muon Solenoid (CMS) are multi-purpose detectors built to search for and measure a wide range of particle interactions and properties. Both experiments measured a particle consistent with the Higgs boson in 2012 and their agreement was a key verification of the discovery. The following sections describe each major component of the ATLAS detector with a focus on their use in the measurement of $\text{Higgs} \rightarrow WW \rightarrow e\nu\mu\nu$.

ATLAS utilizes a coordinate system with its origin at the center of the detector (the “interaction point”) and has a z-axis along the beam pipe. The x-axis points from the interaction point to the center of the LHC ring, and the y-axis points upward. The experiment uses cylindrical coordinates (r, ϕ) where ϕ is the azimuthal angle around the beam pipe. The pseudorapidity and the transverse momentum are defined in terms of the polar angle θ as $\eta = -\ln(\tan(\theta/2))$ and $p_T = p \sin \theta$.

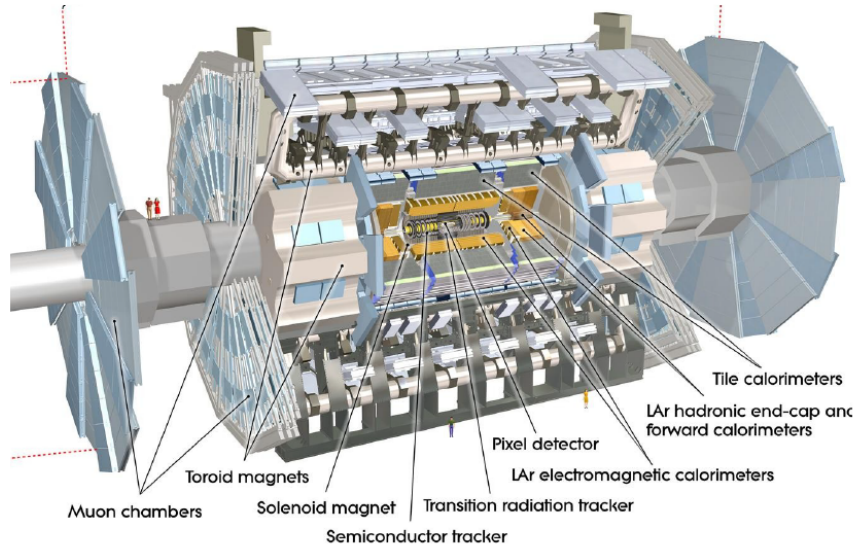


Figure 3.3: Computer-simulated ATLAS detector schematic [??]

The Inner Detector (ID) detects charged particles with an $|\eta| < 2.5$ operating in a 2T solenoidal field. It consists of 3 layers of pixel sensors, 4 layers of silicon strips, and 72

CHAPTER 3. THE LHC AND THE ATLAS DETECTOR

straw layers of transition radiation tracker modules. The ID describes particles closest to the interaction point and detects track parameters with great resolution due to high granularity.

The solenoidal magnet... The toroid magnets....

The Muon Spectrometer precision chambers provide muon momentum measurements at a high resolution over a wide range of p_T . The MS consists of 3 layers of Monitored Drift Tube chambers covering $|\eta| < 2.7$ and an inner layer of Cathode Strip Chambers with $|\eta| > 2.0$. In addition, it includes trigger chambers that contain 3 layers of Resistive Plate Chambers ($|\eta| < 1.05$) and 3 layers of Thin Gap Chambers ($1.05 < |\eta| < 2.4$). As the outermost subdetector, the MS provides precise muon momentum measurements along the muon trajectory and the muon chambers are located with a precision of under $60 \mu m$. The MS also contains a system of three superconducting toroidal magnets each with eight coils providing a magnetic field with a bending integral of up to 6 Tm.

Calorimeters provide detailed information about the energy deposited as particles pass through. Electromagnetic calorimeters detect and halt the motion of electrons and photons while the hadronic calorimeter does the same for hadrons. Muons and neutrinos are able to pass through the calorimeters to the MS. The electromagnetic and hadronic calorimeter, made of liquid Argon and scintillating tiles, respectively, are able to pass information from the location of energy deposits to the muon reconstruction algorithm [??].

3.3 The High-Luminosity LHC and Inner Tracker (ITk)

Though the LHC succeeded in one of its crucial goals of discovering the Higgs boson in 2012, its continuous operation at higher energy and luminosity has led to more rigorous measurements of the Higgs as well as searches for new physics beyond the Standard Model. The LHC has been the leading high energy collider in terms of person power, energy, and scale

CHAPTER 3. THE LHC AND THE ATLAS DETECTOR

for over a decade and will continue to be extremely important for understanding theoretical questions in the future. While more data collection is planned in Run-3 starting in 2021 ??, new colliders and detectors take decades to design, develop and build, so the plans for the collider to take its place is well underway. The High Luminosity LHC will operate at an LHC-level energy (14TeV) and begin data-taking in 2026. The HL-LHC will begin with $5 - 7 \times$ the luminosity of the LHC and will have a design luminosity of $10 \times$ the LHC, or $12.6 \times 10^{-34} \text{cm}^{-2} \text{s}^{-1}$. This huge increase in number of collisions requires massive upgrades to the LHC including new, 11-12T superconducting magnet systems, compact superconducting cavities for beam rotation and phase control, and new technology beam collimation ???. This massive undertaking has been underway for many years already and has involved laboratories all over the world.

Just as the LHC had to be re-designed and built to create higher luminosity, so too do all the experiments on the LHC have to be redesigned to be able to interpret so many more collisions per second. The detectors must be built to withstand more radiation, as the increased collision rate also means a high radiation rate especially closest to the beamline. They also have to provide greater granularity to be able to reconstruct tracks with good enough resolution that individual tracks can be discriminated. Finally, they have to be able to deal with increased pile-up. Pile-up is .. Finally, the increased data in and of itself creates a complex problem for the detectors to solve, as briefly discussed previously, the trigger system must quickly choose which collision events may hold interesting events and store these. When there are more events happening near simultaneously these systems must make these decisions in real-time. New algorithms to speed up this process are necessary when there are an order of magnitude more events to sort through.

Detectors for high energy colliders are not built often- expensive and time-consuming to design and test, they're made to last at least a decade. I was lucky to have the opportunity to

CHAPTER 3. THE LHC AND THE ATLAS DETECTOR

work on ATLAS detector research and development during a year I worked at Brookhaven National Laboratory during my Ph.D. and though my thesis isn't directly related to this work, it was formative and extremely interesting, so I'll touch on this work in the next section. Because I worked on the new ATLAS inner detector for the HL-LHC (termed Inner Tracker or ITk) I will just discuss this sub-detector and the particular role I played in its assembly.

3.3.1 Inner Tracker (ITk)

Building ITk Strip barrel staves

Chapter 4

Tracking and Isolation in ATLAS

4.1 Tracking and isolation in ATLAS

4.1.1 Jets

4.1.2 MET

4.1.3 Electrons

4.1.4 Muons

Muons are abundant in the ATLAS detector and help lead to some of the most interesting physics results and analyses produced by the ATLAS experiment, for example, $H \rightarrow 4\ell$ or $Z' \rightarrow \mu^+\mu^-$ searches (8). The Muon Combined Performance group is tasked with producing the most accurate muon data for physics analyses. This includes muon reconstruction, identification, isolation, and analysis of efficiency, as well as muon momentum scale and resolution. The group’s goal is to create a number of “working points” tailored to different types of physics analyses that will isolate, identify, and reconstruct muons in the region of

CHAPTER 4. TRACKING AND ISOLATION IN ATLAS

interest to the analyses. The working points are continuously updated and improved before being tested and implemented on different analyses. My work with the MCP group has focused on applying corrections necessary for muon momentum scale at the per mille level and resolution at the percent level in simulation/data. These are derived by a template fit of simulations smeared and corrected by variables in data. Finally, these corrections are validated by comparisons to simulations over a variety of variables.

Muon reconstruction is performed independently in the ID and MS and the information from these separate sub-detectors is combined to form full tracks. This section will focus on: 1) reconstruction in the ID, which is the same for any charged particle; 2) reconstruction in the MS, which is particular to muons; and 3) the combined reconstruction, which uses information from both the ID and MS.

Muon reconstruction in the ID

In the ID, a pattern recognition algorithm reconstructs particle tracks with an inside-out sequence (11). A track from a particle traversing the barrel typically has 3 pixel clusters, 8 SCT clusters and more than 30 TRT straw hits. The sequence begins by finding three-dimensional space points from the silicon hits. Each set of three space points which originate in the interaction point are used to trace hits up to the outer edge of the silicon detector. The final track parameters are fit through a collection of hits that extend to the TRT (2).

Muon reconstruction in the MS

Muon reconstruction in the MS is not an inside-out procedure like that in the ID. Reconstruction begins with a search for hit patterns in each MS subdetector, which are called segments. The middle of the MS typically exhibits the largest number of trigger hits, therefore tracks are built by working out from the center of the MS and connecting segments

CHAPTER 4. TRACKING AND ISOLATION IN ATLAS

layer-by-layer. Criteria such as hit multiplicity and fit quality determine track acceptance. At least two segments are needed to build a track. Hits associated with each track candidate are fitted using a global χ^2 fit. A track candidate is accepted if it passes the selection criteria (?).

Combined Reconstruction

The combined ID-MS reconstruction uses different algorithms to find different *muon types*. There are four main types outlined below, but preference in terms of overlap between types is given to Combined (CB), then Segment-tagged (ST), and finally Calorimeter Tagged (CT) muons. These algorithms have been continuously improved to yield better precision, speed, and robustness against misidentification (10).

- **Combined muon (CB):** This type combines tracks from the ID and MS detectors using a global refit on all hits (some may be removed or added to improve quality). Most muons are reconstructed using an outside-in method.
- **Segment-tagged muon (ST):** ST muons are assigned an ID track that is associated with at least one local MDT or CSC track after extrapolation. These are used when muons cross only one layer of the MS because of low p_T or regions out of most MS layer boundaries.
- **Calorimeter-tagged muon (CT):** These muons are identified by an ID track that can be matched to a minimum ionizing particle energy deposit in the calorimeter. These muons have the lowest purity but are optimized for $|\eta| < 0.1$ and $1.5 < p_T < 100$ GeV where the MS is only partially instrumented.
- **Extrapolated muon (ME):** These muons are reconstructed in the MS with the

CHAPTER 4. TRACKING AND ISOLATION IN ATLAS

addition of silicon points and with a loose requirement that the muon track originated at the IP. In general, this muon is required to traverse 2 – 3 layers of MS chambers. These are mainly used to extend acceptance for $2.5 < |\eta| < 2.7$, which is not covered in the ID.

Muon Identification

In order to identify muons from other particles (like backgrounds from pion and kaon decays) strict quality requirements must be set to select prompt muons with high efficiency. Ideal “signal” muons are those that come from W decays (as opposed to light-hadron decays) and originate from the interaction point. We use a few variables to identify muons:

- q/p *significance*: The absolute value of the difference between the ratio of the charge and momentum of muons in the ID and MS divided by the sum in quadrature of their corresponding uncertainties.
- ρ' : The absolute value of the difference between the p_T measurements in the ID and MS divided by the p_T of the combined track.
- χ^2 : The normalized fit parameter of the combined track.

Specific requirements on the number of hits in the ID and MS assure that inefficiencies are expected and momentum measurements are robust. There are four muon identification selections that each addresses specific needs of physics analyses (10).

- **Loose Muons**: The *Loose* criteria maximizes the reconstruction efficiency, losing very few potential muons, while providing satisfactory tracks. All muon types are used in this criteria, and it is the optimal selection for Higgs boson candidates in the four-lepton final state (8).

CHAPTER 4. TRACKING AND ISOLATION IN ATLAS

- **Medium Muons:** *Medium* is the default selection for muons in ATLAS because it minimizes systematic uncertainties associated with reconstruction and calibration. Only CB and ME tracks are used with requirements for over 3 hits in at least two MDT layers in most regions. All *Medium* muons are included in the *Loose* criteria.
- **Tight Muons:** *Tight* selects muons with the highest purity, but sacrifices efficiency. All *Tight* muons are included in the *Medium* selection, but only CB muons with at least two hits in the MS are considered, and the χ^2 value must be less than 8.
- **High- p_T Muons:** *High- p_T* muons have good momentum resolution for tracks with $p_T > 100$ GeV. This is beneficial to searches for high-mass Z' and W' resonances. CB muons in the *Medium* selection with at least 3 hits in 3 MS stations are included.

Muon Reconstruction Efficiency

We measure the muon reconstruction efficiency in two different ways in the regions $|\eta| < 2.5$ and $2.5 < |\eta| < 2.7$. First, in the barrel region, we use the **Tag-and-Probe** method. In this method we select an almost-pure sample of J/ψ and Z decays. We require the leading muon to be a *Medium* muon labeled the **tag**. This muon fires the trigger. The subleading muon, the **probe**, must be reconstructed independently. There are three types of probes:

- **ID track:** Allows measurement of MS efficiency and of tracks not accessible to CT muons.
- **CT tracks:** Allows measurement of MS efficiency and has powerful rejection of background (especially at low p_T). This is the most commonly used probe.
- **MS tracks:** Allows measurement of ID and CT efficiency.

CHAPTER 4. TRACKING AND ISOLATION IN ATLAS

To find the overall efficiency of *Medium*, *Tight*, or *High- p_T* muons, we multiply the efficiencies associated with each type of probe. The efficiency $\epsilon(X|CT)$ ($X = \textit{Medium} / \textit{Tight} / \textit{High-}p_T$) of reconstructing these muons assuming a reconstructed ID track is measured using a CT muon as probe. This result is corrected by the efficiency $\epsilon(ID|MS)$ of the ID track reconstruction measured using MS probes.

$$\epsilon(X|ID) \cdot \epsilon(ID) = \epsilon(X|CT) \cdot \epsilon(ID|MS) \quad (X = \textit{Medium}/\textit{Tight}/\textit{High-}p_T)$$

The ID track reconstruction efficiency must be independent from the muon spectrometer track reconstruction ($\epsilon(ID) = \epsilon(ID|MS)$). In addition, the use of a CT muon as a probe instead of an ID track must not affect the probability for *Medium*, *Tight*, or *High- p_T* reconstruction ($\epsilon(X|ID) = \epsilon(X|CT)$). These assumptions are largely true with simulations showing some small deviations. These deviations are taken into account when calculating systematic errors. The reconstruction efficiency of *Loose* muons is measured separately for CT muons within $|\eta| < 0.1$ and all other *Loose* types. The CT muon efficiency is measured using MS probe tracks, and the efficiency of other muons is evaluated similarly to the *Medium*, *Tight*, and *High- p_T* muons using CT probe muons (10). For $|\eta| > 2.5$, the efficiency is calculated using the ME muons in the **Loose** and **Medium** selections. The number of muons observed in this region is normalized to the number of muons observed in the region $2.2 < |\eta| < 2.5$. A more detailed discussion of the efficiency measurement in this region can be found in Ref. (old). **Scale factors** are defined as the ratios between the efficiency of data and the efficiency of Monte Carlo simulations. They are used to describe the deviation between simulated and real detector behavior and are used in physics analyses to correct simulations.

Figure 4.1 displays reconstruction efficiency for *Medium* muons over a range of p_T and η . J/ψ decays probe low p_T muons while Z decays probe muons of a higher p_T allowing a large

CHAPTER 4. TRACKING AND ISOLATION IN ATLAS

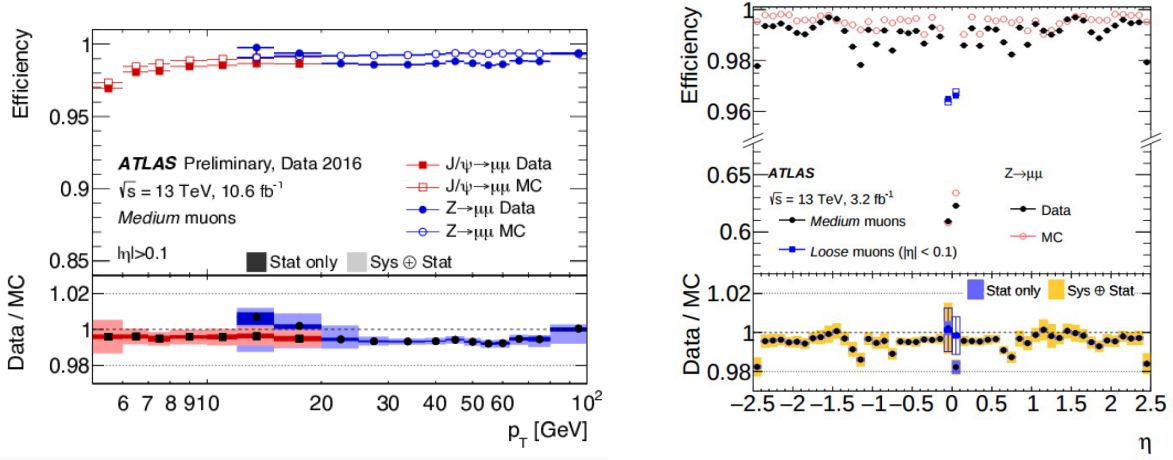


Figure 4.1: On the left, reconstruction efficiency for *Medium* muons from $Z \rightarrow \mu\mu$ and $J/\psi \rightarrow \mu\mu$ events is displayed as a function of the p_T of the muon in the region $0.1 < |\eta| < 2.5$. On the right, muon reconstruction efficiency is shown as a function of η in $Z \rightarrow \mu\mu$ events for muons with $p_T > 10$ GeV for *Medium* and *Loose* muons (squares) in the region $|\eta| < 0.1$, where the *Loose* and *Medium* selections differ significantly. In both plots the error bars on the efficiencies indicate the statistical uncertainty and the bottom panels show the ratio of the measured to predicted efficiencies, with both statistical and systematic uncertainties (10).

range to be defined. Muon reconstruction works well over a large range of both p_T and η as evidenced by an efficiency above 95% throughout ranges shown in p_T and η . In addition, MC simulations match data quite well - within 1 – 2%. The only significant loss of efficiency is seen with *Medium* muons at extremely low η due to criteria excluding ID muons. We can make up this lost efficiency by substituting *Loose* muons for excluded ID muons. Overall, the default *Medium* muon selection demonstrates a high reconstruction efficiency.

Muon Isolation

Isolating muons from heavy particles is one of the keys to understanding the background in many physics analyses. When heavy particles like W , Z , and Higgs bosons decay they often produce muons in isolation. Semileptonic decays, on the other hand, typically

CHAPTER 4. TRACKING AND ISOLATION IN ATLAS

produce muons embedded in jets.

The MCP group uses two muon isolation variables: a track-based variable ($p_T^{varcone30}$) and a calorimeter-based variable ($E_T^{topocone20}$). $p_T^{varcone30}$ is defined as the scalar sum of the transverse momenta of tracks with $p_T > 1$ GeV in a cone around the muon of transverse momentum p_T excluding the muon track itself. The cone size is p_T -dependent to improve the performance for muons produced in decays with a large transverse momentum. $E_T^{topocone20}$ is defined as the sum of the transverse energy of topological clusters in a cone around the muon after subtracting the contribution from the energy deposit of the muon itself and correcting for pile-up effects (9).

Table ?? defines seven isolation selection criteria - called “isolation working points” - that optimize different physics analyses. The *LooseTrackOnly* and *FixedCutTightTrackOnly* working points are defined by cuts on the relative track-based isolation variable. All other working points are defined by cuts applied separately on both relative isolation variables. All cuts are tuned as a function of the η and p_T of the muon to obtain a uniform performance. The target efficiencies of the different working points are described in Table 4.1. The efficiencies for the seven isolation working points are measured in data and simulation using the **Tag-and-Probe** method described in Section 4.1.4 on $Z \rightarrow \mu\mu$ decays. Figure 4.2 shows the isolation efficiency measured for *Medium* muons in data and simulation as a function of the muon p_T for two different working points. In both the *Loose* and *LooseTrackOnly* working points, efficiency is above 98% and matches simulation well within errors.

Muon Momentum Corrections

The muon momentum scale and resolution are studied using Z and J/ψ decays. In order to obtain agreement between simulation and data in muon momentum scale to the per mille level and in resolution to the percent level, we need to apply a set of corrections to the

CHAPTER 4. TRACKING AND ISOLATION IN ATLAS

Isolation WP	Discriminating variable(s)	Definition
<i>LooseTrackOnly</i>	$p_T^{\text{varcone30}}/p_T^\mu$	99% efficiency constant in η and p_T
<i>Loose</i>	$p_T^{\text{varcone30}}/p_T^\mu, E_T^{\text{topocone20}}/p_T^\mu$	99% efficiency constant in η and p_T
<i>Tight</i>	$p_T^{\text{varcone30}}/p_T^\mu, E_T^{\text{topocone20}}/p_T^\mu$	96% efficiency constant in η and p_T
<i>Gradient</i>	$p_T^{\text{varcone30}}/p_T^\mu, E_T^{\text{topocone20}}/p_T^\mu$	$\geq 90(99)\%$ efficiency at 25 (60) GeV
<i>GradientLoose</i>	$p_T^{\text{varcone30}}/p_T^\mu, E_T^{\text{topocone20}}/p_T^\mu$	$\geq 95(99)\%$ efficiency at 25 (60) GeV
<i>FixedCutTightTrackOnly</i>	$p_T^{\text{varcone30}}/p_T^\mu$	$p_T^{\text{varcone30}}/p_T^\mu < 0.06$
<i>FixedCutLoose</i>	$p_T^{\text{varcone30}}/p_T^\mu, E_T^{\text{topocone20}}/p_T^\mu$	$p_T^{\text{varcone30}}/p_T^\mu < 0.15, E_T^{\text{topocone20}}/p_T^\mu < 0.30$

Table 4.1: The seven isolation working points are described by their discriminating variables and defining criteria (10).

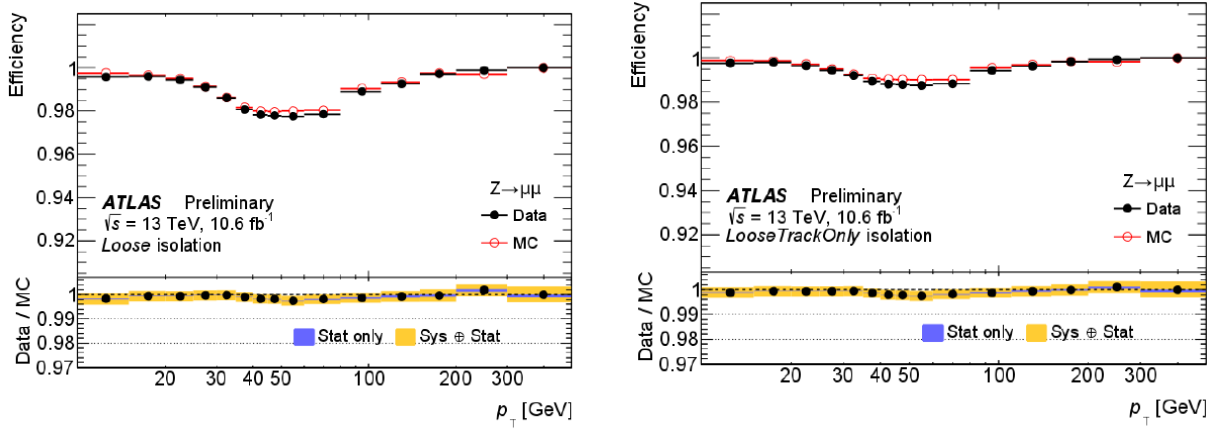


Figure 4.2: Isolation efficiency for the Loose (left) and LooseTrackOnly (right) muon isolation working points. The efficiency is displayed as a function of p_T in $Z \rightarrow \mu\mu$ events. The black markers show efficiency measured in data samples while the red show MC simulations. The bottom panel shows the ratio of the efficiency between the two as well as both statistical and systematic uncertainties (10).

simulated muon momentum. After applying the corrections we validate them by comparing the muon momentum scale and resolution between simulation and data over η , ϕ , and p_T .

I have been heavily involved in calculating the parameters that govern the muon momentum corrections and validating them with the newest datasets. Within the next section, I will describe muon momentum corrections and the parametrizations that define

CHAPTER 4. TRACKING AND ISOLATION IN ATLAS

them.

We extract the calibration parameters with the transverse momentum of the ID and MS components of a CB track. The corrected transverse momentum is described by the following equation:

$$p_T^{\text{Cor,Det}} = \frac{p_T^{\text{MC,Det}} + \sum_{n=0}^1 s_n^{\text{Det}}(\eta, \phi) (p_T^{\text{MC,Det}})^n}{1 + \sum_{m=0}^2 \Delta r_m^{\text{Det}}(\eta, \phi) (p_T^{\text{MC,Det}})^{m-1} g_m}.$$

Here the g_m terms are normally distributed random variables with zero mean and unit width. The Δr and s terms describe momentum resolution smearing and scale corrections applied in specific detector regions, respectively. Both the ID and MS are divided into 18 pseudorapidity regions and the MS is divided into two ϕ bins separating the large and small sectors. Each of these bins leverages different alignment techniques and has different material distributions.

There are two s terms that represent different types of corrections. s_1 corrects for inaccuracy in the description of the magnetic field integral and the detector in the direction perpendicular to the magnetic field. s_0 corrects for the inaccuracy in the simulation of energy loss in the calorimeter and other materials. Since this loss is negligible in the ID, it is only nonzero in the MS (10).

The denominator introduces momentum smearing which broadens the p_T resolution in simulation. The parametrization of the smearing is defined:

$$\frac{\sigma(p_T)}{p_T} = r_0/p_T \oplus r_1 \oplus r_2 \cdot p_T.$$

CHAPTER 4. TRACKING AND ISOLATION IN ATLAS

In this equation r_0 is related to the fluctuations in energy loss in the traversed material, r_1 accounts for multiple scattering, local magnetic field inhomogeneities, and local radial displacements of hits, and r_2 describes intrinsic resolution effects caused by the spatial resolution of the hit measurements and by residual misalignment of the MS (10).

Correction parameters are extracted from data using a binned maximum-likelihood fit with templates derived from simulation which compares the invariant mass distributions for J/ψ and Z decay candidates in data and simulation. The muons are carefully selected to be compatible with tracks that start at the interaction point and penetrate both the ID and the MS. Muons are also selected to pass specific momentum and isolation criteria. The dimuon mass distribution of these tracks in data is fitted using a Crystal Ball function convoluted with an exponential background distribution in the ID and MS fits. The background model and its normalization are then used in the template fit. The fits are performed in $\eta - \phi$ regions of fit (ROFs) which compromise regions with uniform features in the ID and MS (10).

From these fits, we can find the smearing terms across all η regions. Once the corrections are applied we can validate that the agreement between data and MC is excellent. This is shown in Figure 4.3. r_0 is set to zero across all η regions since energy loss is negligible in the ID. r_1 and r_2 increase as η increases since spatial resolution decreases and inhomogeneities increase as we move from the barrel to end-cap regions of both the ID and MS.

We must continue to study muon momentum corrections during ATLAS runs to validate muon calibration performance and account for discrepancies.

CHAPTER 4. TRACKING AND ISOLATION IN ATLAS

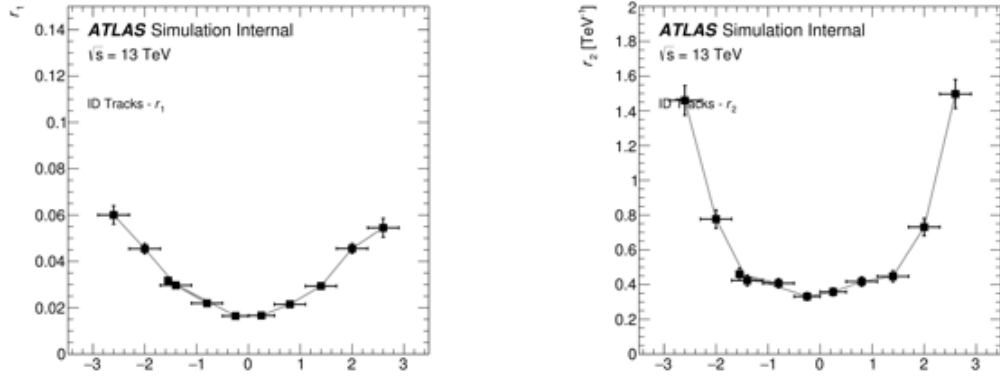


Figure 4.3: The r - values from each of 10 fits of resolution to p_T for ID muon simulations are shown. Each value corresponds to a particular ROF or η region. These plots show r_1 (left) and r_2 (right) as functions of leading muon η .

Chapter 5

Event Selection

5.1 Data and Monte Carlo samples

5.2 Object definitions

5.3 Event selection

Chapter 6

Backgrounds and Systematics

6.1 Backgrounds

6.2 Systematic uncertainties

Chapter 7

Results

7.1 Statistical analysis

7.2 Unfolding

7.3 Results and ratio measurements

Chapter 8

Conclusions

Place your conclusion here.

Bibliography

[old]

- [2] (2010). Performance of the ATLAS Silicon Pattern Recognition Algorithm in Data and Simulation at $\sqrt{s} = 7$ TeV. Technical Report ATLAS-CONF-2010-072, CERN, Geneva.
- [3] (2019). Search for squarks and gluinos in final states with jets and missing transverse momentum using 139 fb^{-1} of $\sqrt{s} = 13$ TeV pp collision data with the ATLAS detector. Technical Report ATLAS-CONF-2019-040, CERN, Geneva.
- [4] Aaboud, M., Aad, G., Abbott, B., Abdinov, O., Abeloos, B., Abhayasinghe, D., Abidi, S., AbouZeid, O., Abraham, N., Abramowicz, H., and et al. (2019a). Cross-section measurements of the higgs boson decaying into a pair of τ -leptons in proton-proton collisions at $\sqrt{s}=13$ tev with the atlas detector. *Physical Review D*, 99(7).
- [5] Aaboud, M., Aad, G., Abbott, B., Abdinov, O., Abeloos, B., Abhayasinghe, D., Abidi, S., AbouZeid, O., Abraham, N., Abramowicz, H., and et al. (2019b). Measurements of gluon–gluon fusion and vector-boson fusion higgs boson production cross-sections in the $h \rightarrow ww^* \rightarrow e\nu\mu\nu$ decay channel in pp collisions at $\sqrt{s}=13$ tev with the atlas detector. *Physics Letters B*, 789:508–529.
- [6] Aaboud, M., Aad, G., Abbott, B., Abdinov, O., Abeloos, B., Abidi, S., AbouZeid, O.,

BIBLIOGRAPHY

- Abraham, N., Abramowicz, H., Abreu, H., and et al. (2018a). Measurements of higgs boson properties in the diphoton decay channel with 36 fb^{-1} of pp collision data at $\sqrt{s} = 13 \text{ tev}$ with the atlas detector. *Physical Review D*, 98(5).
- [7] Aaboud, M., Aad, G., Abbott, B., Abdinov, O., Abeloos, B., Abidi, S. H., AbouZeid, O. S., Abraham, N. L., Abramowicz, H., and et al. (2018b). Measurement of the higgs boson coupling properties in the $h \rightarrow zz^* \rightarrow 4\ell$ decay channel at $\sqrt{s} = 13 \text{ tev}$ with the atlas detector. *Journal of High Energy Physics*, 2018(3).
- [8] Aad, G., Abbott, B., Abdallah, J., Abdel Khalek, S., Abdinov, O., Aben, R., Abi, B., Abidi, S., Abolins, M., AbouZeid, O., and et al. (2014). Measurement of the higgs boson mass from the $h \rightarrow \gamma\gamma$ and $h \rightarrow zz^* \rightarrow 4\ell$ channels in pp collisions at center-of-mass energies of 7 and 8 tev with the atlas detector. *Physical Review D*, 90(5).
- [9] Aad, G., Abbott, B., Abdallah, J., Abdelalim, A. A., Abdesselam, A., Abdinov, O., Abi, B., Abolins, M., Abramowicz, H., and et al. (2013). Jet energy measurement with the atlas detector in proton-proton collisions at $\sqrt{s} = 7 \text{ TeV}$. *The European Physical Journal C*, 73(3).
- [10] Aad, G., Abbott, B., Abdallah, J., Abdinov, O., Abeloos, B., Aben, R., Abolins, M., AbouZeid, O. S., Abraham, N. L., and et al. (2016). Muon reconstruction performance of the atlas detector in proton–proton collision data at

$$\sqrt{s}$$

$s = 13 \text{ tev}$. *The European Physical Journal C*, 76(5).

BIBLIOGRAPHY

- [11] Illingworth, J. and Kittler, J. (1988). A survey of the hough transform. *Computer Vision, Graphics, and Image Processing*, 44(1):87 – 116.
- [12] Rossi, L. (2010). Superconductivity: Its Role, Its Success and Its Setbacks in the Large Hadron Collider of CERN. *Supercond. Sci. Technol.*, 23(CERN-ATS-2010-006):034001. 27 p.
- [13] Tanabashi, M., Hagiwara, K., Hikasa, K., Nakamura, K., Sumino, Y., Takahashi, F., Tanaka, J., Agashe, K., Aielli, G., Amsler, C., Antonelli, M., Asner, D. M., Baer, H., Banerjee, S., Barnett, R. M., Basaglia, T., Bauer, C. W., Beatty, J. J., Belousov, V. I., Beringer, J., Bethke, S., Bettini, A., Bichsel, H., Biebel, O., Black, K. M., Blucher, E., Buchmuller, O., Burkert, V., Bychkov, M. A., Cahn, R. N., Carena, M., Ceccucci, A., Cerri, A., Chakraborty, D., Chen, M.-C., Chivukula, R. S., Cowan, G., Dahl, O., D’Ambrosio, G., Damour, T., de Florian, D., de Gouvêa, A., DeGrand, T., de Jong, P., Dissertori, G., Dobrescu, B. A., D’Onofrio, M., Doser, M., Drees, M., Dreiner, H. K., Dwyer, D. A., Eerola, P., Eidelman, S., Ellis, J., Erler, J., Ezhela, V. V., Fetscher, W., Fields, B. D., Firestone, R., Foster, B., Freitas, A., Gallagher, H., Garren, L., Gerber, H.-J., Gerbier, G., Gershon, T., Gershtein, Y., Gherghetta, T., Godizov, A. A., Goodman, M., Grab, C., Gritsan, A. V., Grojean, C., Groom, D. E., Grünewald, M., Gurtu, A., Gutsche, T., Haber, H. E., Hanhart, C., Hashimoto, S., Hayato, Y., Hayes, K. G., Hebecker, A., Heinemeyer, S., Heltsley, B., Hernández-Rey, J. J., Hisano, J., Höcker, A., Holder, J., Holtkamp, A., Hyodo, T., Irwin, K. D., Johnson, K. F., Kado, M., Karliner, M., Katz, U. F., Klein, S. R., Klempt, E., Kowalewski, R. V., Krauss, F., Kreps, M., Krusche, B., Kuyanov, Y. V., Kwon, Y., Lahav, O., Laiho, J., Lesgourgues, J., Liddle, A., Ligeti, Z., Lin, C.-J., Lippmann, C., Liss, T. M., Littenberg, L., Lugovsky, K. S., Lugovsky, S. B., Lusiani, A., Makida, Y., Maltoni, F., Mannel, T., Manohar, A. V., Marciano,

BIBLIOGRAPHY

W. J., Martin, A. D., Masoni, A., Matthews, J., Meißner, U.-G., Milstead, D., Mitchell, R. E., Mönig, K., Molaro, P., Moortgat, F., Moskvic, M., Murayama, H., Narain, M., Nason, P., Navas, S., Neubert, M., Nevski, P., Nir, Y., Olive, K. A., Pagan Griso, S., Parsons, J., Patrignani, C., Peacock, J. A., Pennington, M., Petcov, S. T., Petrov, V. A., Pianori, E., Piepke, A., Pomarol, A., Quadt, A., Rademacker, J., Raffelt, G., Ratcliff, B. N., Richardson, P., Ringwald, A., Roesler, S., Rolli, S., Romaniouk, A., Rosenberg, L. J., Rosner, J. L., Rybka, G., Ryutin, R. A., Sachrajda, C. T., Sakai, Y., Salam, G. P., Sarkar, S., Sauli, F., Schneider, O., Scholberg, K., Schwartz, A. J., Scott, D., Sharma, V., Sharpe, S. R., Shutt, T., Silari, M., Sjöstrand, T., Skands, P., Skwarnicki, T., Smith, J. G., Smoot, G. F., Spanier, S., Spieler, H., Spiering, C., Stahl, A., Stone, S. L., Sumiyoshi, T., Syphers, M. J., Terashi, K., Terning, J., Thoma, U., Thorne, R. S., Tiator, L., Titov, M., Tkachenko, N. P., Törnqvist, N. A., Tovey, D. R., Valencia, G., Van de Water, R., Varelas, N., Venanzoni, G., Verde, L., Vinciter, M. G., Vogel, P., Vogt, A., Wakely, S. P., Walkowiak, W., Walter, C. W., Wands, D., Ward, D. R., Wascko, M. O., Weiglein, G., Weinberg, D. H., Weinberg, E. J., White, M., Wiencke, L. R., Willocq, S., Wohl, C. G., Womersley, J., Woody, C. L., Workman, R. L., Yao, W.-M., Zeller, G. P., Zenin, O. V., Zhu, R.-Y., Zhu, S.-L., Zimmermann, F., Zyla, P. A., Anderson, J., Fuller, L., Lugovsky, V. S., and Schaffner, P. (2018). Review of particle physics. *Phys. Rev. D*, 98:030001.